



Charge transfer due to defects in hexagonal boron nitride/graphene heterostructures: An *ab initio* study

Madhava Krishna Prasad ^{1,2} Oras A. Al-Ani,^{1,3} Jonathan P. Goss,^{1,*} and Jonathan D. Mar^{1,2,†}

¹*School of Mathematics, Statistics and Physics, Newcastle University, Newcastle upon Tyne, NE1 7RU, United Kingdom*

²*Joint Quantum Centre Durham-Newcastle, United Kingdom*

³*Electrical Engineering Technical College, Middle Technical University, 10011, Baghdad, Iraq*

 (Received 22 December 2022; revised 26 March 2023; accepted 25 August 2023; published 12 September 2023)

Using density functional theory (DFT), we study charge transfer between hexagonal boron nitride (h-BN) point defects and graphene in h-BN/graphene heterostructures using illustrative examples of intrinsic defects: nitrogen vacancy, boron vacancy, nitrogen antisite, and boron antisite. We show that traditional methods that calculate charge transfer by spatial discrimination of charge to different atoms suffer from the misallocation of charge and introduce an alternative method that relies on the integration of the density of states (DOS). We also show that DFT calculations of charge transfer have cell size dependencies due to a change in the DOS in the vicinity of the defect levels. Our results indicate that the nitrogen and boron antisites do not participate in charge transfer, whereas the nitrogen and boron vacancies experience the transfer of a whole electron. Additionally, we show that a change in the geometry of a defect corresponds to a change in the charge state of the defect. The results of this paper will be important for a wide variety of device applications that involve charge transfer between h-BN defects and graphene in h-BN/graphene heterostructures, while our methodology can be feasibly extended to a wide range of point defects and heterostructures.

DOI: [10.1103/PhysRevMaterials.7.094003](https://doi.org/10.1103/PhysRevMaterials.7.094003)

I. INTRODUCTION

As the first two-dimensional (2D) van der Waals material to be realized, graphene has been the focus of an intense research effort due to its extraordinary properties, impacting a wide range of applications in electronics, sensing, medicine, and energy [1–7]. As a natural complementary material to graphene, hexagonal boron nitride (h-BN) has been combined with graphene to form van der Waals heterostructures, leading to a variety of device physics and applications. Examples include graphene devices with very high mobility and very low carrier inhomogeneity [8–10], graphene spintronic devices with long spin-relaxation times and efficient spin injection using h-BN as a substrate/encapsulation layer or tunnel barrier [11–13], and graphene field-effect transistors and twistrionic devices where h-BN is used to modify the band structure of graphene [14,15], to name just a few.

In many of these device applications which employ h-BN/graphene (h-BN/Gr) heterostructures, charge transfer involving defects that are inevitably present in h-BN is a critical factor in device performance and operation. For example, charge transfer resulting in the creation of charged

traps in h-BN may act as Coulombic scattering centers, lowering carrier mobilities and spin-relaxation times in graphene [16,17]. Using charge transfer in h-BN defects as a resource, spin-dependent tunneling in magnetic tunnel junctions has been enhanced due to resonant tunneling through magnetic defect states in an intermediate h-BN layer [17,18]. Additionally, charge transfer has been used to spectrally and spatially quench single-photon emission from h-BN defects when deposited on functionalized [19] and patterned [20] graphene, respectively. Therefore, given the key role that it plays in a wide range of device applications, a detailed theoretical study of charge transfer involving h-BN point defects in h-BN/Gr heterostructures is of fundamental importance. However, such a detailed theoretical study is still lacking in the literature.

Here, we use density functional theory (DFT) to study charge transfer between h-BN point defects and graphene in h-BN/Gr heterostructures for a range of intrinsic defects. Traditional methodologies of determining the degree of charge transfer involve integration of the charge density distribution. However, we show that such methods suffer from errors due to the misallocation of charge since no principled way of allocating charge to an atom exists. We therefore propose an alternative methodology of quantifying the degree of charge transfer that circumvents this issue by using the method of integration of the density of states (DOS). We also show that DFT calculations of charge transfer have cell size dependencies due to a change in the DOS in the vicinity of the defect levels. We apply the proposed methodology to a range of intrinsic defects, chosen as illustrative examples of cases with and without charge transfer. Our findings show that the nitrogen and boron antisites are examples of systems

*jonathan.goss@newcastle.ac.uk

†jonathan.mar@newcastle.ac.uk

Published by the American Physical Society under the terms of the [Creative Commons Attribution 4.0 International](https://creativecommons.org/licenses/by/4.0/) license. Further distribution of this work must maintain attribution to the author(s) and the published article's title, journal citation, and DOI.

that do not participate in charge transfer, whereas the nitrogen and boron vacancies are examples of whole electron transfer. The degree of charge transfer is converged with cell size and is supported by calculations of the band structure and the position of the ionization energies of the defects with respect to the work function of graphene. We also show that a change in the geometry of a defect in a h-BN/Gr heterostructure is consistent with a change in the charge state of the defect.

II. METHODOLOGY

Our DFT calculations were performed using the AIMPRO [21] with periodic boundary conditions and the PBE-GGA exchange-correlation functional [22].

Atoms are modeled using norm-conserving separable pseudopotentials [23], with $1s$ states of B, C, and N parts of the core.

Kohn-Sham eigenfunctions are represented with a basis of sets of independent s - and p -Gaussian orbitals with four different exponents centered on atomic sites [24], with the addition of one (two) sets of d -Gaussian functions for C (B and N) atoms to account for polarization. This amounts to 18 independent Gaussian functions per C atom in the basis and 28 per B and N atoms. Additional sets of functions are located in the vacuum regions to ensure accurate representation of the evanescence. The charge density is Fourier transformed using plane waves with an energy cutoff of 300 Ha, leading to energies converged to better than 1 meV with respect to this parameter.

The Brillouin zone of the primitive structures were sampled using a 16×16 k -point grid and the Monkhorst-Pack scheme [25]. Nonprimitive cells are modeled using grids with a comparable or denser reciprocal space density.

Structures were optimized by the conjugate-gradient method until the total energy changed by $<10^{-5}$ Ha, and forces are $<10^{-4}$ a.u.

The spacing between monolayers was set to 30 a.u. (15.89 Å), which is approximately five interlayer spacings of bulk h-BN [26] for both the monolayer and heterostructure models.

The optimized in-plane lattice constant of monolayer h-BN was calculated to be 2.514 Å, in good agreement with previous comparable calculations and with the experimental value of 2.504 Å [27–30]. Similarly, our calculated value of 2.47 Å for the lattice constant of monolayer graphene is in excellent agreement with the literature [26]. The reproduction of the geometric parameters and band structures (band-structure data are presented in Sec. III) of these monolayer systems provides confirmation that the basis sets, sampling, and treatment of vacuum are sufficiently accurate to provide confidence in the calculated properties of the more complex systems at the center of this paper.

Here, van der Waals interactions were represented using the Grimme-D3 scheme [31]. As monolayer h-BN and graphene have different in-plane lattice constants, a decision regarding the treatment of the lattice constants for heterostructures needed to be made. We have adopted the approach of using a fixed value obtained from the optimization of the in-plane lattice constant for the combined system. This lies between the values of the two isolated systems at 2.49 Å,

representing 1% compressive and tensile strains for h-BN and graphene, respectively.

The formation energy of a defect X in a specific charged state q is

$$E_f(X, q) = E_{\text{tot}}(X, q) - E_{\text{host}} - \sum_i n_i \mu_i + q(\varepsilon_{\text{VBM}} + \varepsilon_F),$$

where $E_{\text{tot}}(X, q)$ is the total energy of the defective supercell of h-BN, E_{host} is the total energy of pristine monolayer h-BN of the same size, n_i is the change in the number of atoms of species i relative to pure h-BN, and μ_i is the chemical potential of the species i . The formation energies were calculated for the N-rich condition specified by $\mu_{\text{N}} + \mu_{\text{B}} = \mu_{\text{h-BN}}$, where μ_{N} is half the total energy of an N_2 molecule, and $\mu_{\text{h-BN}}$ is the energy per formula unit of monolayer h-BN. Here, ε_F is the electron chemical potential relative to the host valence band maximum (VBM), denoted as ε_{VBM} .

We have adopted the standard (q/q') notation to denote the charge transition level (CTL) between charges q and q' relative to the VBM.

Periodic boundary conditions, especially for polarized and charged systems, lead to well-known systematic errors. Additionally, charged defects in an anisotropic system, like monolayer h-BN, are electrostatically screened in-plane but unscreened across the vacuum [32,33]. Correction techniques generally involve extrapolating properties to the dilute limit using data from a range of cell sizes [34,35]. We have adopted the uniform scaling of the cell sizes of Refs. [33,36], leading to an uncertainty of the order of ± 0.1 eV in the formation energy [36] (see Sec. S1 in the Supplemental Material [37]). As we consider defects with low charged states, the maximum charge being $|2e|$, we find that the uncertainty in the valence band position due to the artificial electrostatic field from the charged defect is negligible.

Finally, total electron spin was included as a free parameter during self-consistency and optimization of defect-containing heterostructures, with the total spin reflecting the population of the spin channels based upon Fermi-Dirac statistics with spin-up and spin-down channels having the same self-consistent electron chemical potential. Noninteger spins are found in many cases of small supercells, reflecting the partial charge transfer. The role of the band occupation including spin is explored in Sec. IV.

Quantification of charge transfer has been approached in two ways. The first is by integrating the DOS of the heterostructure from the Fermi level to the small band gap induced by the formation of the heterostructure. For simplicity, we have performed the integration over the majority spin DOS to obtain the population of free carriers in graphene. This region reflects the charge depleted (transferred) from (to) the Dirac cone. The second involves allocating charge density into h-BN and graphene components by dividing the space between the two materials according to the location of the minimum in the average planar charge density.

Then the integrated charge density in each half is allocated to h-BN or graphene, as appropriate. A uniform mesh density which was sufficient to converge the total charge in the supercell to $10^{-2}e$ was used.

The net charge in each volume is the difference between the integrated electron density and the ion charges and the degree

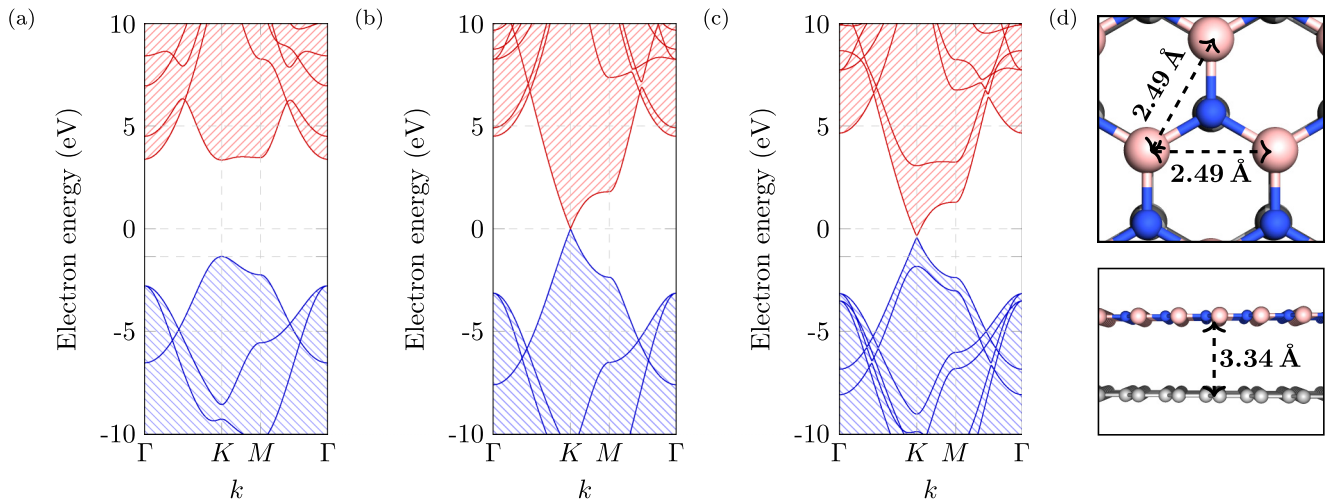


FIG. 1. Calculated band structures in the vicinity of the Fermi energy along high-symmetry branches of the Brillouin zone for (a) monolayer h-BN, (b) monolayer graphene, and (c) an h-BN/graphene heterostructure. Blue and red lines represent nominally occupied and empty bands, respectively, with the underlying shading highlighting the envelopes of the valence and conduction bands. The zero on the energy scale is the Dirac point in pristine graphene, with the other systems aligned so their vacuum levels coincide. (d) Structure of the h-BN/graphene heterostructure, annotated with relevant lengths. Blue, pink, and gray spheres represent N, B, and C atoms, respectively.

of charge transfer is the difference in the total charge of each layer from the monolayer case.

The degree of charge transfer quoted has been converged with cell size to two decimal places. As we shall show, we find that the degree of charge transfer converges with cell size significantly faster using the integration of DOS than integration of charge density. We explore the dependence of the degree of charge transfer on cell size in Sec. IV.

III. RESULTS

A. Pristine h-BN, graphene, and h-BN/graphene heterostructure

The calculated band structure of pristine h-BN is shown in Fig. 1(a), which shows a band gap of 4.6 eV, in agreement with comparable calculations [30]. This is an underestimate compared with the experimental value of 6.1 eV [38], which is a well-known effect of DFT-PBE calculations [39], but we note the valence band dispersion is consistent both with comparable modeling and angle-resolved photoemission spectroscopy measurements [30,40,41]. The ionization energy of h-BN was found to be 5.9 eV, also in agreement with comparable calculations [42].

The calculated band structure of graphene, shown in Fig. 1(b), exhibits the Dirac cone at the K point in accordance with experiment [43]. The work function of graphene was calculated to be 4.3 eV, comparable with the experimental value of 4.6 eV and other PBE-GGA calculations [44,45].

Figure 1(c) shows the h-BN/Gr band structure, showing it can be understood as a simple superposition of the band structures of the individual layers. However, a ~ 0.1 eV band gap opens up near the Dirac point, in agreement with existing literature [46].

The baseline degree of charge transfer in the pristine heterostructure was negligible. The deviation from zero for the defective cases indicates charge transfer. We can now proceed

to the analysis of the defective cases of isolated h-BN and the h-BN/Gr heterostructure.

B. The nitrogen vacancy V_N

The removal of a single nitrogen atom results in a nitrogen vacancy. Here, V_N has been optimized in an h-BN monolayer in several charge states and cell sizes. We find that V_N^+ , V_N^- , and V_N^0 possess D_{3h} symmetry and favor low spin states, in agreement with literature [47–49]. Also, V_N leads to three in-gap states in each spin channel, in agreement with literature [47]. The band structures of the vacancies studied in this paper are shown in Sec. S3 in the Supplemental Material [37]. In the spin-up channel, there is a degenerate unoccupied state close to the conduction band and a singly occupied nondegenerate level ~ 2.5 eV above ϵ_{VBM} . In the heterostructure, the corresponding gap level is depopulated. The heterostructure system favors a singlet state, corresponding to V_N^+ and a nonmagnetic configuration of a partially occupied Dirac cone [Fig. 2(a)]. To further illustrate the association of the bands near the Fermi energy with the defect, Fig. 2(b) shows the same band structure where each state is denoted as h-BN or graphene based upon Mulliken populations: red circles indicate bands more localized in the h-BN layer, and blue circles indicate bands more localized in the graphene layer. Therefore, it is clear that the defect level is localized in h-BN.

The calculated (0/+) level is 1.9 eV, placing it 4.0 eV below vacuum; (–/0) lies at 3.9 eV, which is 2.0 eV below vacuum. Both levels lie above the work function of graphene and are in good agreement with previous calculations [42,50]. Energetically, the location of the (0/+) level suggests electron transfer to the graphene layer should occur, consistent with the band structure and spin state. Furthermore, the calculated net charge of the defective h-BN is $+e$ in the heterostructure, indicating that a whole electron was transferred to the graphene layer. The structure of the defect in the heterostructure is

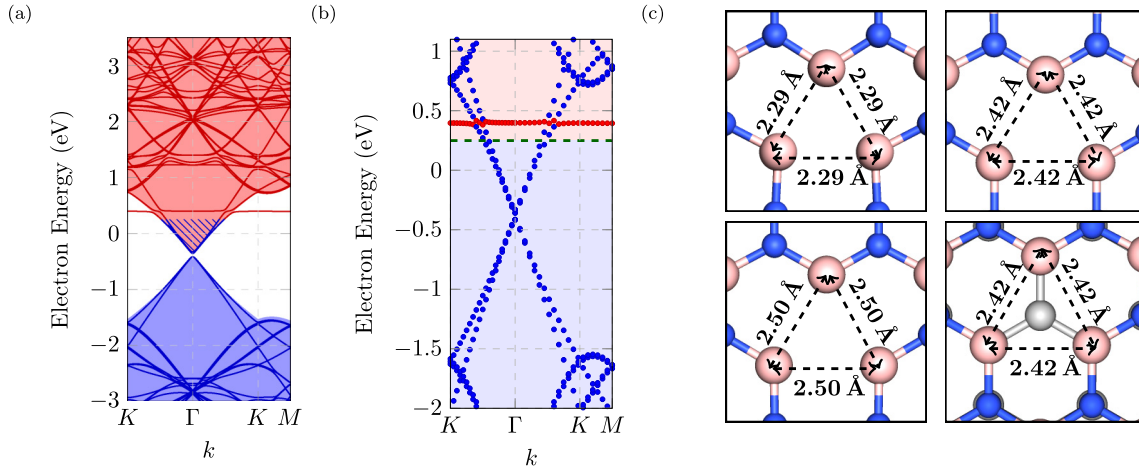


FIG. 2. (a) Band structure of V_N in h-BN/Gr. The hatched shading in (a) indicates the filling of the graphene bands up to the Fermi level, with the underlying shading indicating occupied and empty bands of the corresponding defect-free h-BN/Gr for comparison. (b) Localization of the bands to h-BN (red) or graphene (blue) based upon Mulliken populations. The blue (red) shaded region corresponds to energies below (above) the Fermi level (shown as green dashed line). Colors and scales are as in Fig. 1. (c) Plan-view schematics of V_N^0 (top left) and V_N^{+1} (bottom left) in isolated h-BN, V_N^{+1} in monolayer h-BN with the in-plane lattice constant of that of the heterostructure (top right) and V_N in h-BN/Gr heterostructure (bottom right).

similar to V_N^{+1} in isolated h-BN [Fig. 2(c)], consistent with charge transfer.

Ionizing V_N depopulates bonding orbitals, leading to neighboring B atoms relaxing outward, leading to increased B-B distances [Fig. 2(c)]. The geometry of V_N in the heterostructure resembles that of V_N^{+1} in isolated h-BN, consistent with charge transfer.

C. The boron vacancy V_B

In agreement with previous studies, our optimized ground-state structure for V_B^0 has C_{2v} , arising from a Jahn-Teller distortion [47,51]. Here, V_B acts as an acceptor [48] with the -1 charge state found to be a spin-triplet with D_{3h} symmetry, whereas the -2 charge state is a doublet with C_{2v} symmetry, in agreement with literature [47,48,52].

We find two nondegenerate defect levels in the vicinity of the band gap in each spin channel in the neutral charge case, which agrees with previous modeling [47]. For the majority spin, the lower occupied band is resonant with the top of the valence band, and an unoccupied band is within the band gap. The corresponding spin-minority bands are both unoccupied and within the band gap. In the negative charge state, the higher symmetry leads to a doubly degenerate unoccupied spin-down band deep in the band gap and an occupied degenerate state close to ϵ_{VBM} that mixes with the valence band states, resulting in a multitude of defect-related bands around this energy.

Previous studies [48] indicate V_B is a triple acceptor, and we find single and double acceptor levels at 1.0 eV (4.9 eV below vacuum) and 5 eV [42,48]. The triple acceptor level is very close to the conduction band.

As the calculated $(-)/0$ level of V_B in pristine h-BN is below the work function of graphene, it is thermodynamically favorable for an electron to be transferred from graphene to h-BN.

Figure 3(a) shows the band structure of V_B in the heterostructure. The localization of bands [Fig. 3(b)] confirms the association of the relevant bands to h-BN. The equilibrium geometry of V_B in h-BN/Gr changes from C_{2v} to D_{3h} , which is the symmetry of V_B^{-1} in monolayer h-BN. This change of geometry is consistent with charge transfer having taken place. Results for the geometries for the defects are shown in Sec. S2 in the Supplemental Material [37].

Additionally, calculation of the total charge for each layer confirms the transfer of a whole electron, and the magnetic moment of the defect was found to be $2\mu_B$. We note that this is significantly larger than the degree of charge transfer and magnetic moment found in Ref. [53].

D. The nitrogen antisite N_B

The replacement of a boron atom by a nitrogen atom results in the nitrogen antisite N_B . We find that, in monolayer h-BN, this center favors a spin-singlet in its uncharged state and a doublet in the positive charge state. Neutral N_B possesses an occupied nondegenerate level deep within the band gap, Fig. 4(a) (left). The antisite nitrogen atom moves out-of-plane, resulting in C_{3v} symmetry. As this does not happen for the positively charged case (the defect remains coplanar with the h-BN, yielding D_{3h} symmetry), a change in geometry would be expected if charge transfer involving donation of an electron were to take place.

In h-BN/Gr, the band structure [Fig. 4(a), right] shows the occupied defect band to lie in the band gap, and the antisite nitrogen atom moves out of the h-BN plane. This is consistent with the electrical levels determined for the antisite: the $(0/+)$ level of N_B is calculated at 0.9 eV, which is 5.0 eV below the vacuum, in agreement with literature [42], and hence, the ionization energy of the defect exceeds the work function of graphene. Thus, it is energetically unfavorable for this defect to donate any charge to the neighboring graphene. Indeed, no change in the total charge was calculated in each layer, and

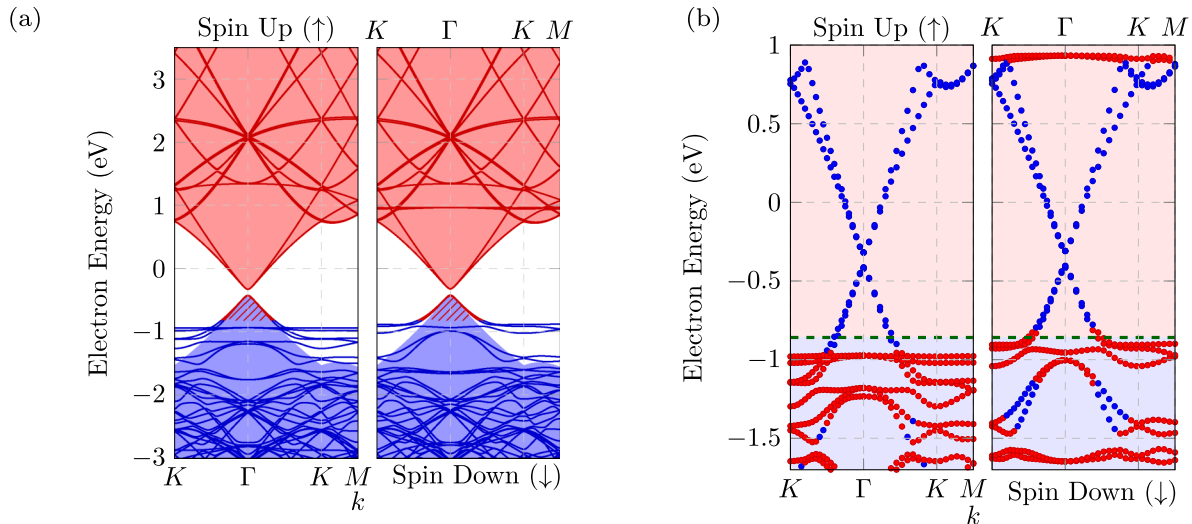


FIG. 3. (a) Band structure of V_B in h-BN/Gr. (b) Mulliken populations analysis. Colors and scales are as in Figs. 1 and 2(b).

the geometry closely resembles the C_{3v} neutral charge state. We therefore conclude that, under equilibrium conditions, N_B would not donate or accept charge with graphene.

E. The boron antisite B_N

Finally, we summarize the results for the boron antisite B_N . Like its nitrogen counterpart, we obtain a spin-singlet ground state in its neutral charge state and a spin-doublet in its ionized state. The introduction of the defect into h-BN leads to three states in the band gap. A doubly degenerate band lies close to ε_{VBM} , and a nondegenerate unoccupied band lies midgap [Fig. 4(b), left].

In h-BN/Gr, the occupied states lie below the band gap [Fig. 4(b), right] and the empty state above, so the band structure indicates charge transfer to be unlikely. Furthermore, $(-/0)$ for B_N is calculated to be 2.8 eV, i.e., 3.1 eV below vacuum, placing the acceptor level well above the work function of graphene. These values of CTLs are consistent with literature [42,48], and the lack of charge transfer is confirmed by the integrated DOS showing negligible change in total charges on the two layers.

IV. DISCUSSION

It is informative to compare charge transfer across the four primary native defects studied. The CTLs of the defect in isolated h-BN with respect to the Dirac point of graphene is a good predictor of the propensity of charge transfer. The CTLs of the antisites are such that there is an energy cost for charge transfer to occur, whereas for vacancies, it is thermodynamically favorable for charge transfer to occur as the donor (acceptor) state lies above (below) the Dirac point in graphene (Fig. 5).

It is also instructive to reflect upon potential impact of the choice of exchange-correlation functional. CTLs of native defects in h-BN obtained using screened-exchange methods (HSE) can be estimated from PBE-GGA values [42]. In Fig. 5, PBE-based CTLs calculated in this paper and the HSE-based

CTLs obtained from Ref. [42] are plotted, where the values are stated relative to the work function of graphene. Despite an increase of ~ 0.4 eV in the energy difference between the hBN VBM and the Dirac point going from PBE to HSE, the differences in the locations of CTLs between PBE-GGA and HSE estimates have been shown to be largely systematic [42], and whether donor and acceptor levels lie above or below the Dirac point is independent of approach for the cases examined. Hence, computation of the propensity for charge transfer between defects in h-BN and graphene can be performed with PBE-GGA functionals to take advantage of the relatively lower computational cost.

We now turn to the key impact of simulation cell size and method of estimate on the degree of charge transfer. For this, we use V_B as a case study.

We begin with the data resulting from the integration of the charge density when dividing the volume into two halves based on the plane containing the minimum of the average charge density. Figure 6(b) shows the degree of charge transfer for two cases. In the absence of the van der Waals correction, the interplane separation is larger (4.2 Å) than with the correction (3.3 Å), and for these data, the average charge density between the graphene and h-BN drops to a very low value. When the van der Waals correction is included, the overlap in the charge density coming from the two materials is much greater, and the minimum value of the charge density between the layers is much greater. In the absence of the van der Waals correction, the integration of the charge density suggests that the transfer of a whole electron would be expected, with the trend in the data suggesting the integrated charge asymptotically approaches one, whereas for the corrected case, the convergence is to a much smaller quantity.

From a fundamental physics point of view, there is no principled way to spatially allocate electron charge to a specific atom, and in this case to either h-BN or graphene. For the cases with different interplane distances, there is a difference in the evanescent drop of charge density, and charge density allocated using proximity suggests that the degree of charge transfer is strongly dependent upon the interplane distance.

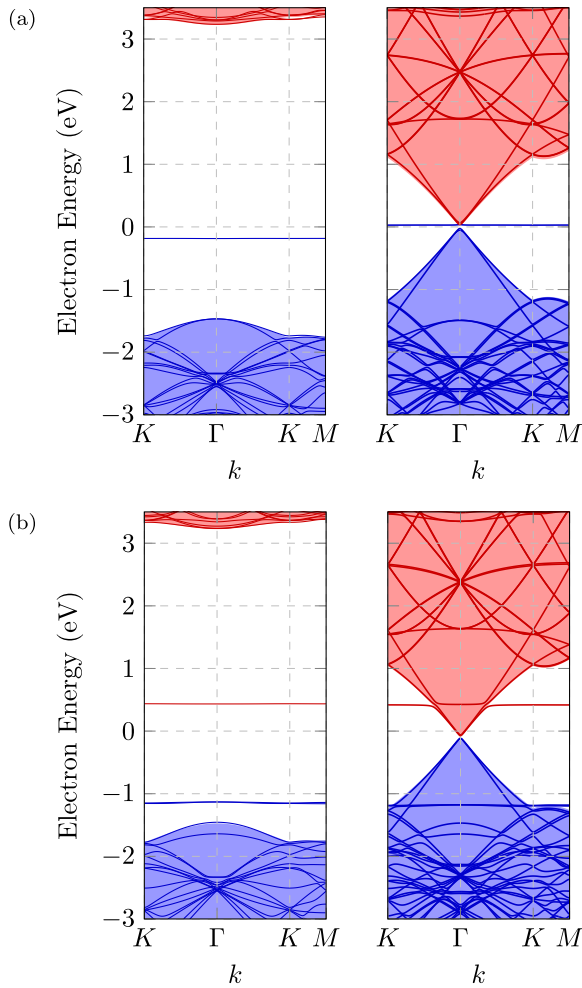


FIG. 4. (a) Band structures of N_B in h-BN (left) and h-BN/Gr (right). (b) Band structures of B_N in h-BN (left) and h-BN/Gr (right).

We now turn to the evaluation of charge transfer based upon the electronic DOS. The use of the electronic DOS is distinct from integration of charge density, as it considers the separation in energy of bands associated with graphene and h-BN. As the CTLs of the point defects examined in this paper lie within a linear regime of the graphene DOS $g(\epsilon)$, we approximated the graphene DOS as $g(\epsilon) = n^2 \lambda \epsilon$, where n is the number of lattice constants in the supercell and λ is the gradient of the primitive pristine graphene DOS, found to be 0.055 eV^{-2} . Then to estimate the cell size required to observe a charge transfer of N electrons, we take a fixed value of the location of the defect CTL and require the graphene DOS between this level and the Dirac point to account for one charge carrier. The integrated DOS is determined as

$$2 \int_0^{\mu_{\text{CTL}}} n^2 \lambda \epsilon d\epsilon = N \Rightarrow n = \frac{1}{\mu_{\text{CTL}}} \sqrt{\frac{N}{\lambda}}. \quad (1)$$

Here, we have taken the Dirac point to be at zero on the electron energy scale, and the factor of 2 represents the spin degeneracy. Then for single electron or hole transfer,

$$n = \left\lfloor \frac{1}{\mu_{\text{CTL}} \sqrt{\lambda}} \right\rfloor. \quad (2)$$

For V_B and for μ_{CTL} located 0.6 eV from the Dirac point, the minimum cell size needed to observe a whole electron transfer would be ~ 50 times larger than the primitive. Figure 6(a) shows the scaling of the DOS near the Dirac point for different cell sizes, illustrating that the integrated DOS between the CTL and the Dirac point increases with cell size. It also shows that there is a minimum cell for which the area under the graphene DOS is sufficient to allow for a whole electron transfer. While the model in Eq. (2) does not consider shifts in the Fermi level occurring due to dispersion in the defect level with supercell size, it remains useful to identify the approximately minimum cell size where the charge transfer obtained by the integration of the DOS will be close to a whole electron. Figure 6(b) shows that the estimate for the minimum size in Eq. (2) is significantly smaller than that implied by the calculated charge transfer from the integrated charge density. However, charge transfer calculated by the integration of the DOS is $\sim 0.9 e^-$ at the minimum cell size predicted by the model.

The DOS model can be developed further by using the electron energy spectra from the heterostructures. For the combined systems, there is a defect band associated with the point defect that exhibits relatively small amounts of dispersion, and for V_B , this lies below the Dirac point of the neighboring graphene. As with the more elementary model DOS approach, as the simulation system size increases, the underlying graphene DOS increases, and the dispersion in the defect band decreases. Once the underlying graphene DOS in the vicinity of the localized V_B band is sufficiently large, the integrated DOS above the defect band exceeds one electron. Once this happens, a whole electron is transferred, filling the localized defect band. Further increases in the simulation system size does not increase the integrated DOS between the Fermi energy and the band gap, as the defect band is filled, and there is no empty DOS associated with the h-BN or defect to populate from the graphene DOS in the vicinity of the Dirac point. Indeed, using the DOS estimate, we found that a cell size $> 12a \times 12a$ showed a whole electron transfer within computational uncertainty [Fig. 6(b)], and even cells as small as $12a \times 12a$ estimate the transfer to be as much as 98% of an electron.

Given that the two approaches yield such significant differences in the estimate of the charge transfer, it is important to resolve which approach, if either, produces the more reliable estimate. To answer this question, we address some properties of the system that are independent of any attempt to separate the charge allocation to graphene or h-BN.

First, if the degree of charge transfer varies with cell size and converges to less than one carrier, as predicted by examination of the spatial variation in the charge density, the total effective electronic spin of these systems would be expected to follow a comparable pattern. Comparing the calculated effective electronic spin plotted in Fig. 7 with the charge transfer estimates in Fig. 6, we see that the degree of charge transfer converges with respect to the cell size at the same rate as the DOS calculations. The effective spin of V_B converges rapidly to $S = 1$, corresponding to the spin state of the negatively charged vacancy in isolated h-BN and consistent with a whole electron transfer from the graphene.

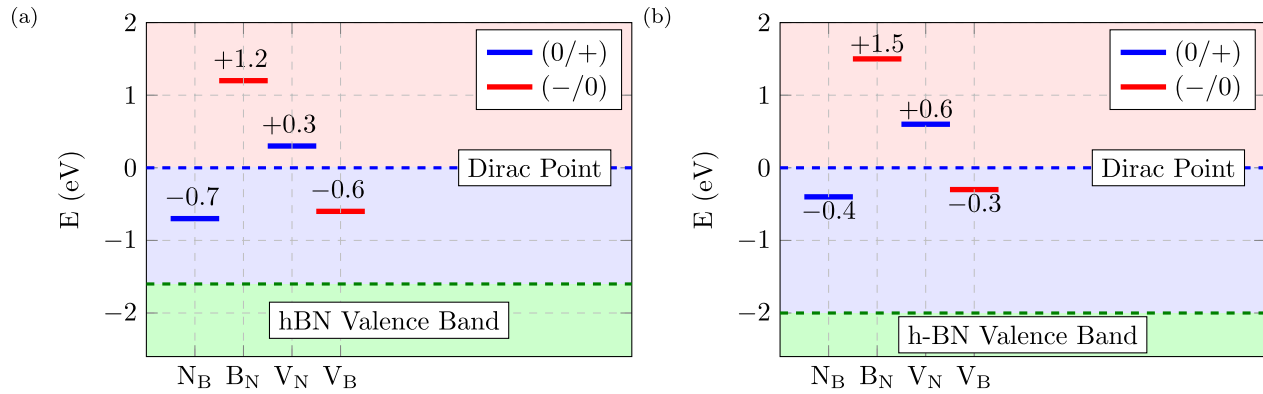


FIG. 5. Charge transition levels of defects studied in this paper, calculated using (a) the PBE-GGA functional, relative to the calculated work function of graphene, and (b) HSE CTLs, relative to the experimental work function of graphene. HSE and experimental work functions are indistinguishable on this scale [54,55].

Secondly, band structure and analysis of the electronic orbitals of V_B in h-BN/Gr are consistent with it being in the negative charge state. For example, V_B experiences a Jahn-Teller distortion from D_{3h} to C_{2v} in the neutral charge state in isolated h-BN, whereas the negatively charged spin-triplet case retains the D_{3h} symmetry. In our calculations, the cell-size converged result shows a geometry indistinguishable from the D_{3h} symmetry case in isolated h-BN. All the available data, other than the integrated charge density, point to the defect being fully ionized and not to a situation with a partial charge transfer. This casts some light on the result previously published for charge transfer between graphene and h-BN [53], which predicted 50% of an electron transfer and a total effective spin of $S = 3/4$. This result was obtained using a simulation cell which we show in this paper does not yield a converged effective spin. Furthermore, the method adopted to estimate the charge transfer was based upon the charge density rather than the band structure.

While the DOS method seems to have advantages over methods using the integration of charge density, care must be taken in its application. The DOS method is most beneficial

for cases where there is no significant hybridization of the states near the Dirac point of the graphene layer. The Fermi level of the heterostructure then acts to separate the DOS into distinct graphene and h-BN energy regions. However, in a case where an adsorbate or defect forms a bond with graphene, such as an interstitial, hybridization of the Dirac cone may well occur. In such a case, it is ambiguous as to whether the states corresponding to charge transfer originate from the atom, graphene, or h-BN, and the integration of the DOS is then possibly not an improvement upon a spatial integration of the charge density. This has been illustrated in the Supplemental Material [37] using the boron interstitial.

We also discuss the impact of h-BN states in the integration range between the Fermi level and the band gap. Here, V_B again serves as a useful illustrative example, providing insights into both how one might extract only the graphene DOS and illustrating the impact of insufficiently converged cell sizes.

The band structure of neutral and negatively charged V_B in isolated h-BN (Figs. S4(b) and S4(c) in the Supplemental Material [37]) indicates that the location in energy of the defect

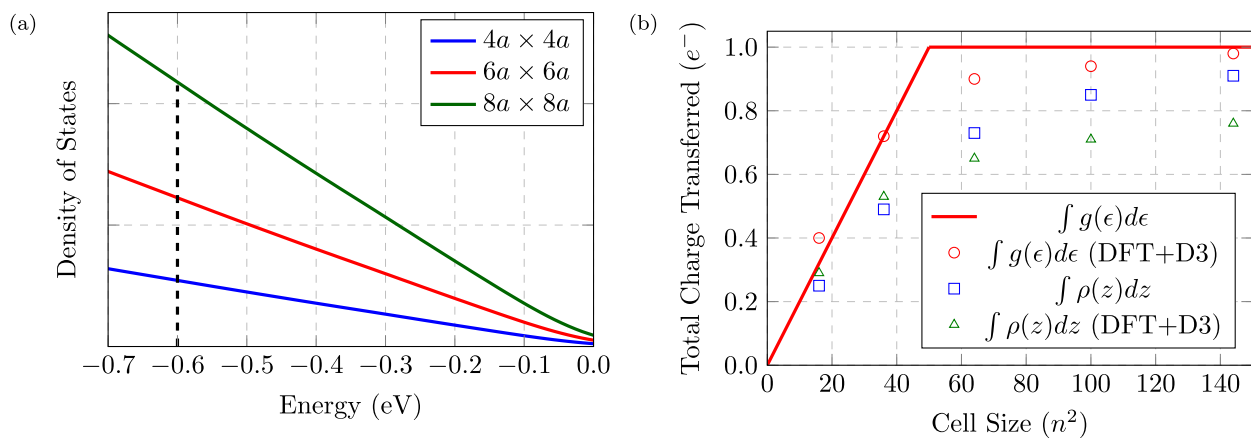


FIG. 6. (a) A plot of the total electronic density of states (DOS) for pristine graphene at the approximately linear region close to the Dirac point. The vertical dotted black line is the $(-/0)$ level of V_B in isolated h-BN relative to the Dirac point in pristine graphene. (b) The degree of charge transfer obtained by the integration of the DOS of graphene and the heterostructure (red line and red circles, respectively) and by the charge density distribution with and without van der Waals forces (blue squares and green triangles, respectively).

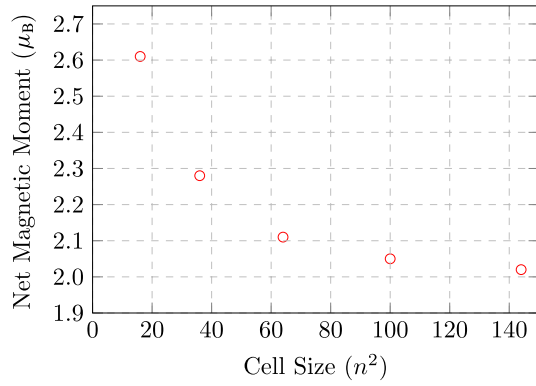


FIG. 7. A plot of μ_B with respect to the cell size for V_B in h-BN/Gr.

bands relative to the Dirac point of the graphene depends upon the occupancy of these bands, which in turn depends upon the cell size. The highest minority-spin band corresponding to h-BN partially lies in the energy range over which one wishes to determine the integrated DOS of graphene [Fig. 3(b)]. Were one to include both majority- and minority-spin channels in the analysis, the unoccupied minority-spin h-BN bands may impact upon the estimate of the integrated graphene DOS. The magnitude of this impact is illustrated in Fig. 8 which shows the calculated charges corresponding to the integration of the DOS from the Fermi level to the Dirac point for each spin channel. The integrated spin-up DOS matches the convergence of the magnetic moment, in contrast to the integral of the total DOS, Fig. 7, a consequence of the presence of h-BN bands around the Fermi level, Fig. 3. In small supercells, the Fermi level needs to lie deep in the Dirac cone to contribute enough states to correspond to a whole electron transfer. However, the presence of higher energy h-BN states in the minority-spin channel sets a limit to the depth of the Fermi level. If the Fermi level lies below this h-BN band, the state is fully unoccupied, leading to more than a whole electron transfer (this is because the h-BN state contributes a whole electron in addition to the depleted graphene states). However, there is a constraint to the total amount of charge that can be transferred, as there is only one acceptor state below the Dirac

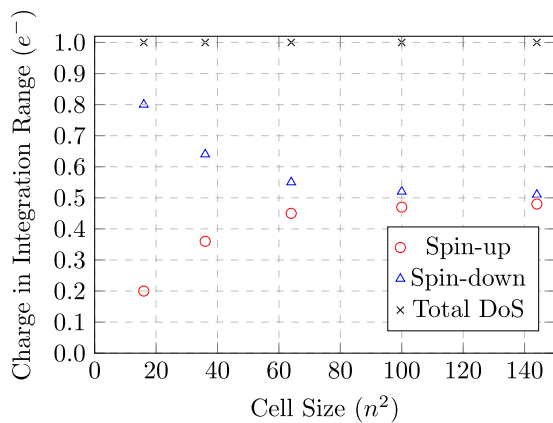


FIG. 8. The total charge in the integration range in the spin-up (red circles) and spin-down (blue triangles) channels, and total density of states (DOS; black crosses) of V_B in h-BN/Gr.

point (the state in the majority-spin channel participating in charge transfer). Therefore, the Fermi level lies at the h-BN band, such that it is partially occupied and the total number of depleted states corresponds to a whole electron regardless of the system size, as seen in Fig. 8. Furthermore, from Fig. 3(b), we can see there are graphene states above the defect band in the majority-spin channel that do not participate in charge transfer due to the location of the Fermi level. From Fig. 3(b), it can be seen that the number of undepleted graphene states approximately equals the depleted h-BN states. It can be envisaged that, if the DFT calculations of the smaller supercells were performed with constrained spin, the Fermi level would lie at different energies in each spin channel such that a whole electron transfer is observed. However, this requires *a priori* knowledge of the expected magnetic moment of the system, and in such a system, the graphene layer would be magnetic. However, in the converged limit, from Figs. 6(b) and 8, it can be seen that the true system should reflect a diamagnetic graphene layer. This means that, in the absence of significant rehybridization of the graphene bands (such as might be present in cases of adatoms and interstitials), the impact of defect bands in the minority-spin channel can be mitigated for by determining the charge corresponding to the spin-up channel and doubling this quantity to account for the spin degeneracy of the graphene states.

V. CONCLUSIONS

In this paper, we have shown that routinely employed methods of determining charge transfer based on spatially allocating charge density result in the misallocation of charge. This becomes especially important in the case of 2D material heterostructures because charge is distributed in the delocalized π states where the distinction between bands associated with dissimilar materials is primarily in terms of their energy rather than their spatial distribution. We therefore adopted an alternative method based on the integration of the electronic DOS, where for the present application, we avoid the error of assigning charge in a spatial location to a plane of atoms by integrating the states which have been depleted (filled) from (in) the donor (acceptor) species. In complete support of this approach, we found that the degree of charge transfer with respect to cell size obtained from the integration of DOS follows closely the convergence of the effective electronic spin in the system, the magnitude of which is closely related to the population of the localized defect states. The magnetic properties are inconsistent with the estimate of the charge transfer from charge density integration.

We also draw conclusions in the context of the specific material system we have analyzed. We have shown that the position of CTLs of defects in h-BN with respect to the work function of graphene can be used to predict the propensity for charge transfer. From calculations of the CTLs, band structure, and quantity of charge transfer, we conclude that N_B and B_N do not undergo charge transfer, whereas V_N and V_B exchange a whole electron with graphene.

Our conclusions are supported by a combination of band structure, integrated charge density, and geometric changes associated with ionized forms of the vacancies.

Critically, there is a clear dependence of charge transfer with supercell dimensions, and there is a need to perform calculations of charge transfer quantification in a sufficiently large cell size to achieve convergence. This is in part a consequence of the localized nature of the states involved in the defects in h-BN as well as the delocalized states in the graphene. It can also be understood in terms of the graphene DOS in the vicinity of the donor or acceptor band of the defect in the heterostructure. For V_B , we found that 12×12 unit cells were sufficiently large to approximate the dilute limit, and we predict that this should be the case for defects where the defect bands have a similar degree of localization and an acceptor/donor level with a similar energy difference from the Dirac point.

Finally, the intrinsic defects studied in this paper serve as prototypes to illustrate the susceptibility of different defects to charge transfer. As the principles presented here apply quite generally in h-BN/Gr heterostructures and the likelihood for charge transfer to take place can be gauged from a knowledge of the location of the donor or acceptor levels relative to the graphene Dirac point, it can be extended to a wider range of defects. For example, carbon substituting for boron has a donor level 2.2 eV above the h-BN VBM [56], placing it 0.6 eV above the Dirac point; therefore, it can be expected that charge transfer will take place in this case.

This can be extended beyond the monolayer case. As h-BN shows a shift in band edge positions as it transitions from a monolayer to bulk h-BN [41], the change in the environment of the defect can lead to different degrees of electrostatic screening experienced by the defect, which can in turn have an impact on the CTLs. The donor level of C_B in bulk h-BN

is 2.8 eV from the VBM, or 1.1 eV above the Dirac point [56], and therefore might be described as more donorlike than in monolayer h-BN. Therefore, a situation can be envisaged where a defect has a donor (acceptor) level below (above) the Dirac point in monolayer h-BN. For such cases, the presence of intermediate layers may shift the CTLs above (below) the Dirac point, allowing charge transfer to take place, so it is relevant for general cases to consider the range of CTLs relevant to the defect centers as a function of both location and number of h-BN layers. For cases where the defects are separated in space from the graphene by a number of intermediate layers, the dynamics as well as the equilibrium energetics of charge transfer will also be of interest.

In this paper, we show that great care is required in the quantitative prediction of charge transfer. Our focus has been upon the thermodynamics of charge transfer to aid the design of a wide range of devices such as spin valves using magnetic defect states for spin-dependent tunneling, single-photon emitters with electrical charge control, and highly sensitive devices for biosensing applications [2,18,57,58]. We note that it would be of interest to develop the modeling further, including necessary time-dependent approaches, to explore the dynamics of charge transfer, such as tunneling rates and excited state lifetimes.

ACKNOWLEDGMENTS

We would like to thank Prof. P. Briddon and Dr. M. Rayson for their support in the usage of AIMPRO for the DFT calculations. M.K.P. gratefully acknowledges financial support from Newcastle University.

-
- [1] E. L. Wolf, *Solar Cells and Electrodes* (Springer International Publishing, Cham, 2014), pp. 39–49.
 - [2] H. Chang, L. Tang, Y. Wang, J. Jiang, and J. Li, *Anal. Chem.* **82**, 2341 (2010).
 - [3] H. Li, S. Ruan, and Y.-J. Zeng, *Adv. Mater.* **31**, 1900065 (2019).
 - [4] A. G. Olabi, M. A. Abdelkareem, T. Wilberforce, and E. T. Sayed, *Renew. Sustain. Energy Rev.* **135**, 110026 (2021).
 - [5] M. Pumera, *Energy Environ. Sci.* **4**, 668 (2011).
 - [6] M. Pumera, *Mater. Today* **14**, 308 (2011).
 - [7] W. Choi, I. Lahiri, R. Seelaboyina, and Y. S. Kang, *Crit. Rev. Solid State Mater. Sci.* **35**, 52 (2010).
 - [8] C. Palacios-Berraquero, *Quantum Confined Excitons in 2-Dimensional Materials* (Springer, Cham, 2018), pp. 71–89.
 - [9] M. Yankowitz, Q. Ma, P. Jarillo-Herrero, and B. J. LeRoy, *Nat. Rev. Phys.* **1**, 112 (2019).
 - [10] C. R. Dean, A. F. Young, I. Meric, C. Lee, L. Wang, S. Sorgenfrei, K. Watanabe, T. Taniguchi, P. Kim, K. L. Shepard *et al.*, *Nat. Nanotechnol.* **5**, 722 (2010).
 - [11] M. H. D. Guimarães, P. J. Zomer, J. Ingla-Aynés, J. C. Brant, N. Tombros, and B. J. van Wees, *Phys. Rev. Lett.* **113**, 086602 (2014).
 - [12] M. Gurram, S. Omar, and B. J. van Wees, *2D Mater.* **5**, 032004 (2018).
 - [13] M. V. Kamalakar, A. Dankert, J. Bergsten, T. Ive, and S. P. Dash, *Sci. Rep.* **4**, 6146 (2014).
 - [14] M. Yankowitz, J. Xue, D. Cormode, J. D. Sanchez-Yamagishi, K. Watanabe, T. Taniguchi, P. Jarillo-Herrero, P. Jacquod, and B. J. LeRoy, *Nat. Phys.* **8**, 382 (2012).
 - [15] G. Giovannetti, P. A. Khomyakov, G. Brocks, P. J. Kelly, and J. van den Brink, *Phys. Rev. B* **76**, 073103 (2007).
 - [16] J. H. Gosling, O. Makarovskiy, F. Wang, N. D. Cottam, M. T. Greenaway, A. Patanè, R. D. Wildman, C. J. Tuck, L. Turyanska, and T. M. Fromhold, *Commun. Phys.* **4**, 30 (2021).
 - [17] U. Chandni, K. Watanabe, T. Taniguchi, and J. P. Eisenstein, *Nano Lett.* **16**, 7982 (2016).
 - [18] P. U. Asshoff, J. L. Sambricio, S. Slizovskiy, A. P. Rooney, T. Taniguchi, K. Watanabe, S. J. Haigh, V. Fal'ko, I. V. Grigorieva, and I. J. Vera-Marun, *Nano Lett.* **18**, 6954 (2018).
 - [19] Z.-Q. Xu, N. Mendelson, J. A. Scott, C. Li, I. H. Abidi, H. Liu, Z. Luo, I. Aharonovich, and M. Toth, *2D Mater.* **7**, 031001 (2020).
 - [20] J. C. Stewart, Y. Fan, J. S. Danial, A. Goetz, A. S. Prasad, O. J. Burton, J. A. Alexander-Webber, S. F. Lee, S. M. Skoff, V. Babenko *et al.*, *ACS Nano* **15**, 13591 (2021).
 - [21] R. Jones and P. Briddon, *Semicond. Semimet.* **51**, 287 (1998).
 - [22] J. P. Perdew, K. Burke, and M. Ernzerhof, *Phys. Rev. Lett.* **77**, 3865 (1996).

- [23] C. Hartwigsen, S. Goedecker, and J. Hutter, *Phys. Rev. B* **58**, 3641 (1998).
- [24] J. P. Goss, M. J. Shaw, and P. R. Briddon, in *Theory of Defects in Semiconductors*, Vol. 104 of Topics in Applied Physics, edited by D. A. Drabold and S. K. Estreicher (Springer, Berlin/Heidelberg, 2007), pp. 69–94.
- [25] H. J. Monkhorst and J. D. Pack, *Phys. Rev. B* **13**, 5188 (1976).
- [26] J. Wang, F. Ma, and M. Sun, *RSC Advances* **7**, 16801 (2017).
- [27] L. Cai, X. Fan, H. Su, M. Lv, and B. Xu, *Ferroelectrics* **566**, 136 (2020).
- [28] B. Xu, M. Lv, X. Fan, W. Zhang, Y. Xu, and T. Zhai, *Integr. Ferroelectr.* **162**, 85 (2015).
- [29] A. Janotti, S.-H. Wei, and D. J. Singh, *Phys. Rev. B* **64**, 174107 (2001).
- [30] M. Topsakal, E. Aktürk, and S. Ciraci, *Phys. Rev. B* **79**, 115442 (2009).
- [31] S. Grimme, *WIREs Comput. Mol. Sci.* **1**, 211 (2011).
- [32] H.-P. Komsa and A. Pasquarello, *Phys. Rev. Lett.* **110**, 095505 (2013).
- [33] H.-P. Komsa, N. Berseneva, A. V. Krasheninnikov, and R. M. Nieminen, *Phys. Rev. X* **4**, 031044 (2014).
- [34] C. W. M. Castleton and S. Mirbt, *Phys. Rev. B* **70**, 195202 (2004).
- [35] H.-P. Komsa, T. T. Rantala, and A. Pasquarello, *Phys. Rev. B* **86**, 045112 (2012).
- [36] H.-P. Komsa, N. Berseneva, A. V. Krasheninnikov, and R. M. Nieminen, *Phys. Rev. X* **8**, 039902(E) (2018).
- [37] See Supplemental Material at <http://link.aps.org/supplemental/10.1103/PhysRevMaterials.7.094003> for the illustration of extrapolation of formation energies; defect geometries of V_B , N_B , and B_N ; band structures of V_N and V_B in monolayer h-BN; and the hybridization of graphene states.
- [38] C. Elias, P. Valvin, T. Pelini, A. Summerfield, C. Mellor, T. Cheng, L. Eaves, C. Foxon, P. Beton, S. Novikov *et al.*, *Nat. Commun.* **10**, 2639 (2019).
- [39] A. J. Cohen, P. Mori-Sánchez, and W. Yang, *Science* **321**, 792 (2008).
- [40] H. Henck, D. Pierucci, G. Fugallo, J. Avila, G. Cassabois, Y. J. Dappe, M. G. Silly, C. Chen, B. Gil, M. Gatti *et al.*, *Phys. Rev. B* **95**, 085410 (2017).
- [41] D. Wickramaratne, L. Weston, and C. G. Van de Walle, *J. Phys. Chem. C* **122**, 25524 (2018).
- [42] X. Liu, Z. Gao, V. Wang, Z. Luo, B. Lv, Z. Ding, and Z. Zhang, *ACS Appl. Mater. Interfaces* **12**, 17055 (2020).
- [43] M. Sprinkle, D. Siegel, Y. Hu, J. Hicks, A. Tejada, A. Taleb-Ibrahimi, P. Le Fèvre, F. Bertran, S. Vizzini, H. Enriquez *et al.*, *Phys. Rev. Lett.* **103**, 226803 (2009).
- [44] Y.-J. Yu, Y. Zhao, S. Ryu, L. E. Brus, K. S. Kim, and P. Kim, *Nano Lett.* **9**, 3430 (2009).
- [45] D. Ziegler, P. Gava, J. Güttinger, F. Molitor, L. Wirtz, M. Lazzeri, A. M. Saitta, A. Stemmer, F. Mauri, and C. Stampfer, *Phys. Rev. B* **83**, 235434 (2011).
- [46] R. M. Torres-Rojas, D. A. Contreras-Solorio, L. Hernández, and A. Enciso, *Solid State Commun.* **341**, 114553 (2022).
- [47] B. Huang and H. Lee, *Phys. Rev. B* **86**, 245406 (2012).
- [48] L. Weston, D. Wickramaratne, M. Mackoik, A. Alkauskas, and C. G. Van de Walle, *Phys. Rev. B* **97**, 214104 (2018).
- [49] A. Sajid, J. R. Reimers, and M. J. Ford, *Phys. Rev. B* **97**, 064101 (2018).
- [50] F. Wu, A. Galatas, R. Sundararaman, D. Rocca, and Y. Ping, *Phys. Rev. Mater.* **1**, 071001(R) (2017).
- [51] V. Ivády, G. Barcza, G. Thiering, S. Li, H. Hamdi, J.-P. Chou, Ö. Legeza, and A. Gali, *npj Comput. Mater.* **6**, 41 (2020).
- [52] J. Strand, L. Larcher, and A. L. Shluger, *J. Phys.: Condens. Matter* **32**, 055706 (2020).
- [53] S. Park, C. Park, and G. Kim, *J. Chem. Phys.* **140**, 134706 (2014).
- [54] V. Barone, J. E. Peralta, J. Uddin, and G. E. Scuseria, *J. Chem. Phys.* **124**, 024709 (2006).
- [55] V. Barone, O. Hod, J. E. Peralta, and G. E. Scuseria, *Acc. Chem. Res.* **44**, 269 (2011).
- [56] D. Wang and R. Sundararaman, *Phys. Rev. B* **101**, 054103 (2020).
- [57] M. Yu, D. Yim, H. Seo, and J. Lee, *2D Mater.* **9**, 035020 (2022).
- [58] S. J. U. White, T. Yang, N. Dontschuk, C. Li, Z.-Q. Xu, M. Kianinia, A. Stacey, M. Toth, and I. Aharonovich, *Light Sci. Appl.* **11**, 186 (2022).